Mechanical characterization of a unidirectional pultruded composite lamina using micromechanics and numerical homogenization

Xin, Haohui; Mosallam, Ayman; Liu, Yuqing; Veljkovic, Milan; He, Jun

DOI
10.1016/j.conbuildmat.2019.04.191

Publication date
2019

Document Version
Final published version

Published in
Construction and Building Materials

Construction and Building Materials 216 (2019) 101–118

Contents lists available at ScienceDirect

Construction and Building Materials

journal homepage: www.elsevier.com/locate/conbuildmat

Mechanical characterization of a unidirectional pultruded composite lamina using micromechanics and numerical homogenization

Haohui Xin [a,b], Ayman Mosallam [c], Yuqing Liu [a,*], Milan Veljkovic [b], Jun He [d]

[a] Department of Bridge Engineering, Tongji University, Shanghai, China
[b] Faculty of Geoscience and Engineering, Delft University of Technology, The Netherlands
[c] Department of Civil & Environment Engineering, University of California, Irvine, USA
[d] School of Civil Engineering, Changsha University of Science & Technology, Hunan, China

HIGHLIGHTS

- A continuum damage model was implemented via user material subroutine to model fiber failure.
- The Mohr-Coulomb plastic criterion were used to model the epoxy behavior.
- The cohesive surfaces were used to simulate the fiber-matrix interface damage.
- Different analytical micromechanics theories were verified by the test results.
- Numerical homogenization methods effectively predicted the pultruded lamina macroscopic properties.

ARTICLE INFO

Article history:
Received 27 February 2018
Received in revised form 13 March 2019
Accepted 23 April 2019
Available online 6 May 2019

Keywords:
Pultruded unidirectional GFRP lamina
Micro-mechanic analysis
Numerical homogenization
Engineering constants
Mohr-Coulomb plastic criterion

ABSTRACT

In this paper, analytical and numerical homogenization methods are proposed to effectively simulate the macroscopic characteristics of a pultruded composite lamina. A continuum damage model was implemented via user material subroutine to model fiber failure, while the Mohr-Coulomb plastic criterion is employed to model matrix damage. In order to simulate the damage of the fiber-matrix interface, the relationship between traction and displacement is established. The proposed theoretical and numerical models were verified by tensile, compressive, and shear test results. The outcomes of this study indicated that both theoretical, numerical prediction values agree well with experimental verification results confirming the validity of the proposed methodology in providing a reliable reference for structural design of pultruded fiber reinforced polymeric (FRP) composite structures.

1. Introduction

Deterioration of existing structures built with traditional materials such as concrete, steel, and timber is considered to be a major challenge for civil engineers. Fiber reinforced polymer (FRP) composites are one of the promising alternative materials that potentially can solve this problem with its unique features such as its high strength-to-weight ratio, and high resistance to harsh environments [1–5]. One of the popular types of composites that have been used by civil engineers for the past three decades or so is manufactured through the pultrusion continuous manufacturing process. Pultruded glass fiber reinforced polymer (GFRP) composites could meet the established design criteria with reasonable cost and are often recommended for newly constructed bridges and buildings [6–9]. Typical pultruded composites profiles used in civil engineering application includes I- and H-shaped girders [1,2], double web beam [10], GFRP-concrete hybrid decks [3,4,11] and modular bridge decks [12,13].

Due to the fact that GFRP composites are inhomogeneous, anisotropic and viscoelastic, such materials require more sophisticated and multi-level (micro-mechanics and macro-mechanics) analytical producers, as compared to conventional materials such as steel, and reinforced concrete. The importance of adopting a multi-scale analysis in determining mechanical properties of pultruded GFRP laminates has been recommended in previous studies e.g. [12,13]. Although several investigations on carbon fiber reinforced polymer (CFRP) for aerospace structures were conducted, results and outcomes of such studies are not generally applicable to pultruded composites that are commonly used in construction applications. One of the known difficulties in modeling pultruded composites accurately [14] is that pultruded composites are not precisely

* Corresponding author.
E-mail address: yql@tongji.edu.cn (Y. Liu).

https://doi.org/10.1016/j.conbuildmat.2019.04.191
0950-0618/

laminated structures due to the nature of the pultrusion process. For this reason, analytical modeling that considers the specific nature of pultruded composites is required in order to predict its thermo-mechanical performance. Details for calculating lamina thickness, laminates fiber volume fraction and engineering constants of each lamina were reported previously by the authors [12,13]. In addition, and in order to accurately obtain lamina strength, laboratory tests to characterize the unidirectional lamina strength are needed. However, the experimental approach is usually impractical due to several reasons including: (i) each lamina is orthotropic that requires measuring multiple strength parameters including: longitudinal tensile strength, X_T, longitudinal compressive strength, X_C, transverse tensile strength, Y_T, transverse compressive strength, Y_c, and in-plane shear strength, S., (ii) as stated earlier, pultruded composites are not precisely laminated in the true sense due to the nature of the manufacturing process and it is physically almost impossible to extract the mechanical properties of an individual lamina experimentally (refer to Fig. 1). For this reason, the micromechanics approach, the technique used to obtain values of composite material, are adopted in this study, where relatively accurate homogenization models are used to predict the equivalent properties of pultruded composites.

Micromechanics models can be classified as analytical and numerical. The analytical methods include empirical, semi-empirical, and strictly-analytical mode. Many analytical techniques of homogenization are based on equivalent Eigen-strain method [15]. The Reuss model [15] (also called *rule-of-mixtures*), assumes that the strain tensors in the fiber, matrix, and composites are the same. The longitudinal elastic modulus E_1 and longitudinal Poisson's ratio v_{12} are derived and computed this way in the rule of mixtures formulas. The *Voigt* model (also called the *inverse rule of mixtures*), assumes that the stress tensors in the fiber, matrix, and composite are the same. The transverse elastic modulus E_2 and in-plane shear modulus G_{12} etc. are derived and computed this way in the inverse rule of mixtures formulas. Considering initial imperfections, the formulas of the *rule of mixtures* were improved by introducing empirical parameter [16]. If the composite could be approximated as having periodic microstructure, then Fourier series could be used to estimate all the components of the stiffness tensor of a composite. Explicit formulas for a composite reinforced by long circular cylindrical fibers, which are periodically arranged in a square array, are adopted by Barbero et al. [17]. In addition to predicting the elastic engineering constants, the rule-of-mixtures approach was also used to predict lamina's longitudinal tensile and longitudinal compressive strength X_T and X_C, respectively [15,18,19]. In this approach, fibers and the matrix are assumed to behave linearly up to failure and the fibers were stiff and brittle relative to the matrix, implying that the longitudinal tensile strength is dominated by fiber strength. The longitudinal compressive failure [15,18] could also be assumed to be dominated by fiber micro-buckling when individual fibers buckle inside the matrix. The transverse tensile strength of composites [18,20] is dominated by matrix ultimate strength that is lower than the matrix strength by a factor (SRF) known as the strength-reduction factor, that depends on the volume fractions properties of fibers and matrix. The transverse compressive strength could be obtained by the strain-magnification factor method [21,22] or by empirical formulas [23,24]. As compared with analytical micromechanics formulations [25], numerical homogenization simulation can consider both geometry and spatial distribution of the phases as well as predicting both damage propagation and failure strength. Numerical homogenization method [26] is an emerging methodology that is considered to be an effective modeling tool for analyzing FRP composites, where the lamina macroscopic properties could be acquired by means of numerical modeling of deformation and failure of the microstructure model. The microstructure is generally called representative volume element (RVE). Results of several research studies conducted on nonlinear simulation of the mechanical response of FRP lamina have been reported. For example, Gonzalez and Lorca [25] analyzed the mechanical response of a unidirectional FRP subjected to transverse compression. The results showed that transverse compression behaviors of unidirectional FRP were mainly controlled by interface strength and the matrix yield strength while the failure modes were controlled by the nucleation of interface cracks or by the formation of matrix shear bands. Vaughan and McCarthy [27] investigate the effect of fiber-matrix debonding and thermal residual stress on the transverse damage behavior of unidirectional FRP. Results of their study indicated that the fiber-matrix interface strongly affected the transverse strength and that the interfacial strength is one of the major controlling factors of the overall transverse strength. Soni et al. [28] developed a three-dimensional micromechanical finite element model to predict mechanical behavior and damage response of composite laminates, where the macroscopic stress-strain fields were obtained using Gauss's theorem, in conjunction with the Hill-Mandal strain energy equivalence principle. The predicted results from the proposed model, which could be used to study the effect of matrix friction angle and cohesive strength of the fiber-matrix interface on global material response. In addition, it could be used to predict initiation and propagation of the fiber-matrix interfacial decohesion and propagation at every point in the laminate, were found to be in good agreement with experimental results. Romanowicz [29] employed the numerical homogenization methods to predict the strength of unidirectional FRP lamina under a combination of the transverse compression and axial tension. The failure modes were found to be mainly due to fiber breakage, fiber/matrix debonding, and matrix plastic deformation. The proposed model is verified against an analytical solution and experimental data. Results showed that the numerical results agreed better with experimental data than the analytical model. Xin et al. [30] conducted numerical homogenization to predict the tensile and shear behavior of steel reinforced resin after validated by compressive material test results. The friction angle, the ratio of the yield stress in triaxial tension to the yield stress in triaxial compression, and the dilation angle of the linear Drucker Prager plastic model are obtained based on experiments and

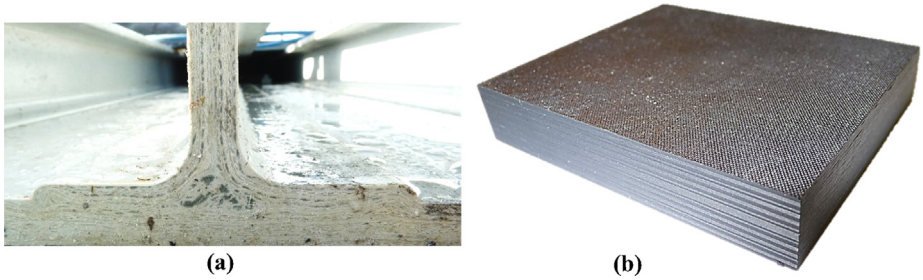

(a) (b)

Fig. 1. Pultruded composites vs. laminated composites.

numerical homogenization simulation. Melro et al. [31] used a pressure-dependent, elasto-plastic thermodynamically consistent damage mode to simulate the matrix and used cohesive elements to model the interface between matrix and fibers. Their results showed that damage initiation is mainly due to interfacial damage under both transverse tension and shear loadings and that the damage initiation under longitudinal shear load is mainly due to the damage of the epoxy matrix. Ullah et al. [32] developed a computational homogenization framework to predict the nonlinear mechanical response of FRP composites. The accuracy and performance of the computational framework are demonstrated with a variety of numerical examples.

In order to expand the use of pultruded GFRP profiles in bridge engineering and provide basic design data of pultruded unidirectional GFRP lamina, analytical and numerical homogenization methods were used to effectively model the lamina macroscopic properties. Continuum damage model implemented via user material subroutine is employed to simulate fiber failure, Mohr-Coulomb plastic criterion is employed to simulate the matrix damage and the cohesive surfaces reflecting the relationship between traction and displacement at the interface were employed to simulate the fiber-matrix interface. Tensile performance, compressive performance and shear performance have been experimentally studied to validate the theoretical and numerical results.

2. Analytical micromechanics evaluation

Based on information obtained from an in-depth literature review conducted in this study, it is believed that there is a dearth of references involving pultruded FRP profiles in civil engineering application with multiscale prediction in both modulus and ultimate capacity.

2.1. Lamina engineering constants

Unidirectional lamina's moduli include longitudinal elastic modulus E_1, transverse elastic modulus E_2, in-plane shear modulus G_{12}, transverse shear modulus G_{23}, longitudinal Poisson's ratio v_{12} and transverse Poisson's ratio v_{23}. The detailed equations to predict lamina engineering constants were listed in Appendix A.

2.2. Lamina ultimate strength

The ultimate strength of a pultruded unidirectional lamina includes longitudinal tensile strength F_{1t}, transverse tensile strength F_{2t}, longitudinal compressive strength F_{1c}, transverse compressive strength F_{2c} and in-plane shear strength S. Detailed equations to predict ultimate strengths were listed in Appendix B. It is also noted that the purpose of predicted strength is to provide initial coarse reference in the finite element simulation in the fact that the constitutive law of sub-materials and interface between sub-materials were much complicated.

3. Computational homogenization

As stated earlier, numerical homogenization simulation could accurately consider the geometry and spatial distribution of the phases, and also could precisely estimate the propagation of damage to accurately predict the failure strength as compared to analytical micromechanics formulations [25].

3.1. Computational homogenization & periodic boundary condition

The link between micro-scale and macro-scale behavior could be established based on Hill-Mandel computational Homogenization method. The macro-scale Cauchy stress $\bar{\sigma}_{ij}$ is obtained by averaging the microscale Cauchy stress, σ_{ij}, in the unit cell domain, expressed as Eq. (1). [26]:

$$\bar{\sigma}_{ij} = \frac{1}{|\Theta|}\int_{\Theta}\sigma_{ij}d\Theta \tag{1}$$

where: $\bar{\sigma}_{ij}$ is the macro-scale Cauchy stress, σ_{ij} is the micro-scale Cauchy stress, Θ is the domain of the unit cell. The unit cell problem could be solved for the leading order translation-free micro-scale displacement. The micro-scale displacement $u_i^f(x,y)$ is expressed in the following form [26]:

$$u_i^f(x,y) = \varepsilon_{ij}^c y_j + u_i^{(1)}(x,y) \tag{2}$$

where: x is the macro-scale position vector in the macro-scale domain, y is the micro-scale position vector in the unit cell domain; ε_{ij}^c is the strain tensors in the macro-scale domain, $u_i^{(1)}(x,y)$ is the perturbation displacement of the micro-scale.

If two nodes, M and S, located at the opposite faces of the RVE model, with M and S being the master and slave nodes respectively. Considering the periodic boundary conditions [26] in the unit cell domain gives:

$$u_i^f\left(x,y_j^M\right) - u_i^f\left(x,y_j^S\right) = \varepsilon_{ij}^c\left(y_j^M - y_j^S\right) \tag{3}$$

This could be implemented by so-called "*mixed boundary conditions*" via constraint equations, is expressed by the following equations [26,33]:

$$\int_{\partial\Theta_\gamma}\left(u_i^f(x,y) - \varepsilon_{ik}^c y_k\right)N_j^\Theta d\gamma_\gamma = 0 \tag{4}$$

$$\left|u_i^f(x,y) - \varepsilon_{ik}^c y_k\right|N_j^\Theta \le Tol \tag{5}$$

where: N_j^Θ is the unit normal to the unit cell boundary $\partial\Theta_y$.

3.2. Material constitutive model

Typical *RVE* model in the case of unidirectional GFRP composites employed in this paper is shown in Fig. 2, which consists of a fiber embedded in a matrix polymer. The macro-scale GFRP material behavior could be obtained by averaging micro-scale stress distribution and considering individual sub-materials components constitutive law and fiber-matrix interface de-bonding. Each constitutive model of sub-material is detailed explained as below section.

3.2.1. Fibers

In this study, a continuum damage material model was implemented via the user-material subroutine UMAT of ABAQUS/

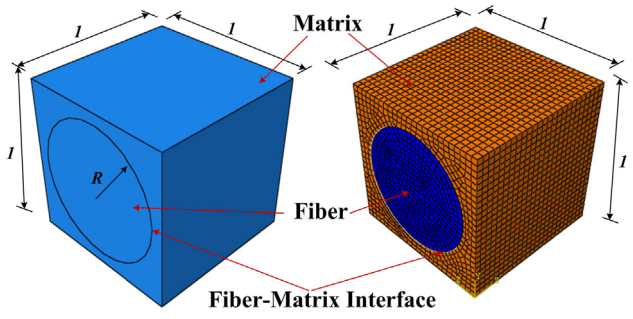

Fig. 2. Typical RVEs of unidirectional FRP composites.

Standard [34] to simulate the fiber damage. The stress and strain relationship [12] was expressed as follows:

$$\sigma_{ij} = (1 - w)L_{ijkl}\varepsilon_{kl} \tag{6}$$

where: w is the damage variable. Once a damage initiation is detected, further loading will cause degradation of material stiffness. The stiffness reduction coefficients are dependent on damage variables. The evolution of damage variable, w, is assumed to be governed by equivalent strain $\hat{\varepsilon}$. Now, considering the brittle nature of glass fibers, the glass fibers are assumed to be fully damaged when the equivalent strain, $\hat{\varepsilon}$, increases to a value larger than the defined strain threshold value $t\varepsilon_f^u$. The damage variable is given as the following relationship:

$$\Upsilon(\hat{\varepsilon}) = \begin{cases} 0 & \hat{\varepsilon} < {}^t\varepsilon_f^u \\ w_{\max} & \hat{\varepsilon} \geq {}^t\varepsilon_f^u \end{cases} \tag{7}$$

where: $w_{\max}$ is the maximum value of the damage variable and is assumed to be 0.999 in this manuscript to avoid convergence problems. The equivalent strain, $\hat{\varepsilon}$, is defined as follows:

$$\hat{\varepsilon} = \sqrt{\frac{2}{3}\sum_{i=1}^{3}\left\langle \bar{\varepsilon}_i \right\rangle^2} \tag{8}$$

where: $\bar{\varepsilon}_i$ is the principal strain in each direction. Note that the shear strain is zero in the principal strain coordinate. The operator "< >" is defined in order to consider the difference between tensile damage and compressive damage of glass fibers. The effective principal strain, $\left\langle \bar{\varepsilon}_i \right\rangle$, in each direction is given as the following relationship:

$$\left\langle \bar{\varepsilon}_i \right\rangle = \begin{cases} \bar{\varepsilon} & \bar{\varepsilon}_i \geq 0 \\ \chi\bar{\varepsilon} & \bar{\varepsilon}_i < 0 \end{cases} \tag{9}$$

where: the material parameter χ is defined as the ratio of the ultimate tensile strain to the ultimate compressive strain.

$$\chi = \frac{t\varepsilon_f^u}{c\varepsilon_f^u} \cong \frac{t\sigma_f^u}{c\sigma_f^u} \tag{10}$$

where: $t\sigma_f^u$ and $c\sigma_f^u$ is the ultimate tensile and compressive strength of fibers.

The yield function that predicts damage initiation of glass fibers is expressed by the following relation:

$$g(\hat{\varepsilon}, r) = \hat{\varepsilon} - r \leq 0 \tag{11}$$

The loading functions obey the loading-unloading conditions of the Karush–Kuhn–Tucker conditions, and are expressed in the following form [14]:

$$\dot{\omega} \geq 0, g(\hat{\varepsilon}, r) \leq 0, \dot{\omega}g(\hat{\varepsilon}, r) = 0 \tag{12}$$

Materials models with softening behavior and stiffness degradation generally have convergence difficulties in implicit finite element method. In order to alleviate convergence difficulties, a viscous regularization scheme is adopted, and a viscous damage variable is defined by the evolution equations [14]:

$$\dot{w}^v = \frac{1}{\eta}(w - w^v) \tag{13}$$

where: η is a viscosity coefficient representing the relaxation time of the viscous system and w^v denotes regularized damage variable.

The finite element equations obtained for this model by discretizing the virtual work equations are in general nonlinear, and the Newton–Raphson technique is used to solve the resulting system of nonlinear equations in ABAQUS [34]. It is important to note that the material tangent constitutive tensor is computed correctly to ensure the robustness of the Newton–Raphson method. The material tangent constitutive tensor could be computed from the following equation:

$$\frac{\partial\sigma_{ij}}{\partial\varepsilon_{kl}} = (1 - w^v)L_{ijkl} \tag{14}$$

The detailed implementation algorithm is summarized in Table 1.

Table 1
Implementation algorithm of fiber damage model.

1 Initial variable: $\{{}^n w, {}^n w^v, {}^n r\}$
2 Update strain : ${}^{n+1}\varepsilon_i = {}^n\varepsilon_i + \Delta\varepsilon_i \quad i = 1 \ldots 6$
3 Compute the principal strain ${}^{n+1}\bar{\varepsilon}_j \quad j = 1 \ldots 3$
4 Compute the equivalent strain ${}^{n+1}\hat{\varepsilon}$
5 Update stress and Jacobian Matrix:
5-1 If ${}^{n+1}\hat{\varepsilon} \leq {}^n r$*:*
$${}^{n+1}r = {}^n r,\ {}^{n+1}w = {}^n w,\ {}^{n+1}w^v = {}^n w^v$$
5-2 If ${}^{n+1}\hat{\varepsilon} > {}^n r$*:*
$${}^{n+1}r = {}^{n+1}\hat{\varepsilon},\ {}^{n+1}w = \Upsilon({}^{n+1}\hat{\varepsilon}),\ {}^{n+1}$$
$${}^{n+1}w^v = \frac{\eta}{\eta+\Delta t}{}^n w^v + \frac{\Delta t}{\eta+\Delta t}{}^{n+1}w$$
5-3:Update Stress:
$${}^{n+1}\sigma_{ij} = (1 - {}^{n+1}w)L_{ijkl}^{n+1}\varepsilon_{kl}$$
5-4:Update Jacobian Matrix:
$${}^{n+1}\left(\frac{\partial\sigma_{ij}}{\partial\varepsilon_{kl}}\right) = (1 - {}^{n+1}w)L_{ijkl}$$

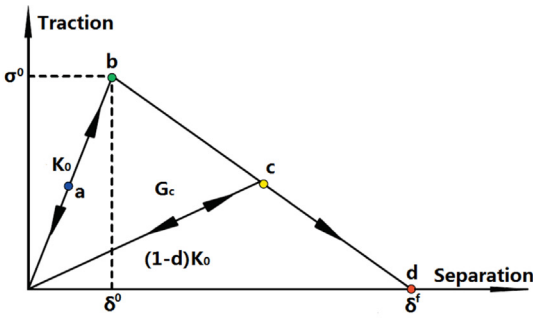

(a) Bilinear constitutive law

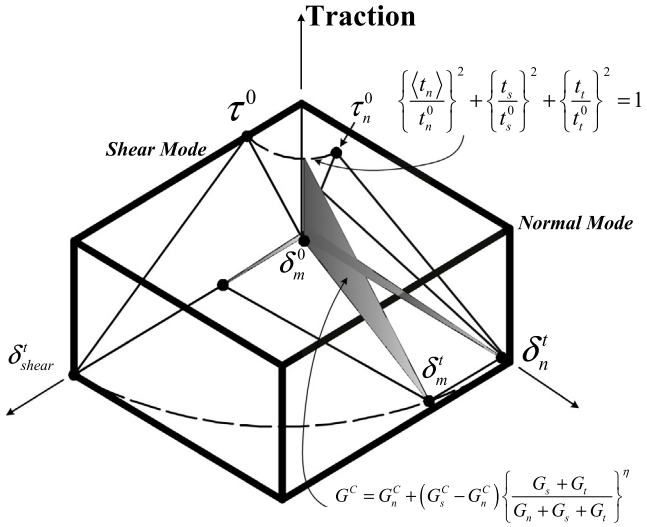

(b) Mixed-mode response of cohesive elements

Fig. 3. Illustration of material model.

Table 2
Mechanical properties of E-glass fibers.

Longitudinal modulus, E_{f1} (GPa)	Transverse modulus, E_{f2} (GPa)	Poisson's ratio, υ_f	Shear modulus, G_f (GPa)	Tensile strength, X_{ft} (MPa)	Compressive strength, X_{fc} (MPa)	Density, ρ (kg/m^3)
74.0	74.0	0.20	30.80	2150	1450	2560

Table 3
Mechanical properties of epoxy resin.

Modulus, E_m (GPa)	Poisson's ratio, υ_m	Shear modulus G_m, (GPa)	Tensile strength X_{mt}, (MPa)	Compressive strength, X_{mc}, (MPa)	Shear strength, S_m, (MPa)	Density (ρ), (kg/m^3)
3.35	0.35	1.24	80.0	120.0	75.0	1160

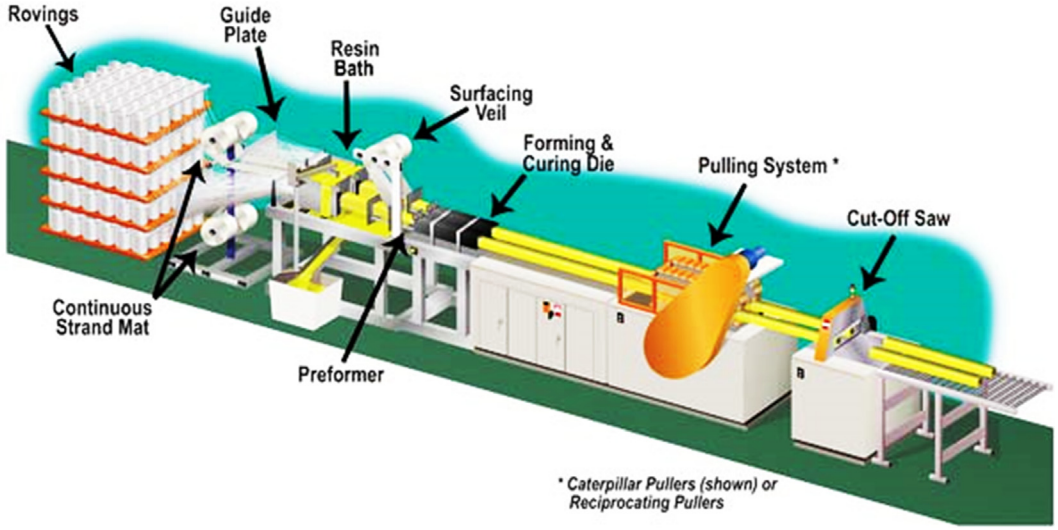

Fig. 4. Schematic of the pultrusion process [38].

Table 4
Fiber volume fraction and density.

Number	Length (mm)	Width (mm)	Thickness (mm)	Mass *before* burning, (g)	Mass *after* burning, (g)	Composite destiny, (kg/m^3)	Fiber fraction (%)
1	24.12	25.11	4.2	4.84	3.65	1902.7	56.1%
2	24.95	23.93	4.05	4.05	3.50	1931.3	56.5%
3	25.00	23.47	4.22	4.22	3.55	1926.4	56.0%
Average	24.69	24.17	4.16	4.37	3.56	1920.1	56.2%

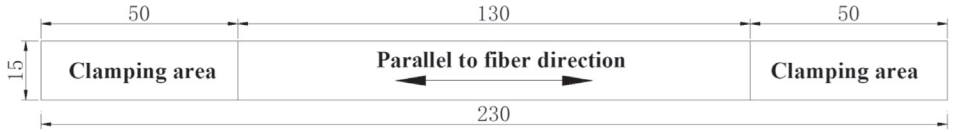

(a) Longitudinal tensile

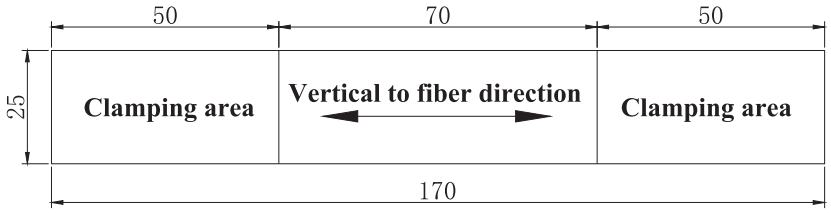

(b) Transverse tensile

Fig. 5. Tensile specimen (mm).

3.2.2. Polymer matrix

The polymeric matrix was assumed to behave as isotropic materials. The plastic behavior of the polymer matrix was assumed to be governed by the Mohr-Coulomb criterion [34,35]. The Mohr-Coulomb criterion assumes that the yielding happens when the shear stress along one specific plane reaches a critical value, which is related to the normal stressσ. It is expressed as:

$$\tau = c - \sigma\tan\phi \tag{15}$$

where: c stands for the cohesion of the matrix materials, ϕ stands for the friction angle of the matrix materials. The cohesion, c, stands for the failure stress under pure shear while the friction angle ϕ is used to consider the effects of the hydrostatic stress on yield stress. The values of both material parameters could be determined from its tensile and compressive strengths, σ_{mt} and σ_{mc} expressions as follow:

$$\sigma_{mt} = 2c\frac{\cos\phi}{1+\sin\phi} \tag{16}$$

$$\sigma_{mc} = 2c\frac{\cos\phi}{1-\sin\phi} \tag{17}$$

The Mohr-Coulomb yield surface can then be expressed as [34]:

$$F = R_{mc}q - p\tan\phi - c = 0 \tag{18}$$

where: p is the hydrostatic stress, q is the Mises equivalent stress, R_{mc} is defined as the Mohr-Coulomb deviatoric stress measure, the detailed expression may refer to [34].

3.2.3. Fiber-matrix interface

The cohesive surfaces reflecting the relationship between traction and displacement at the interface were employed to simulate the fiber-matrix interface. As shown in Fig. (3-a), the bilinear traction-separation model, which assumed to be linear elastic (point "*a*") followed by the damage initiation (point "*b*"), the evolution of damage (point "*c*"), and finally the fully damaged state (point "*d*"), is employed in this paper. In the elastic stage [12,13], the traction increased linearly along with the displacement with an initial slope of K_0. At point "*b*", the damage of the cohesive element is initiated. The cohesive element is always subjected to combined loading including opening, in-plane shear and out-of-plane shear, the quadratic stress failure criterion [34] is used to evaluate the initial damage, as is shown in Fig. (3-b).

$$\left\{\frac{\langle t_n\rangle}{t_n^0}\right\}^2 + \left\{\frac{t_s}{t_s^0}\right\}^2 + \left\{\frac{t_t}{t_t^0}\right\}^2 = 1 \tag{19}$$

where: t_n , t_s and t_t are traction components related to pure modes *I*, *II* and *III*, t_n^0, t_s^0 and t_t^0 are interfacial strength of pure modes *I*, *II* and *III*.

In the damage evolution period, the interfacial stiffness degraded from initial K_0 to (1-d) K_0, where d is a damaged variable. The Benzeggagh-Kenane fracture criterion (BK Law) described in Eq. (20) [34,36] is particularly used to predict damage propagation of mixed-mode loadings in terms of the critical fracture energies during deformation purely along with the first and the second shear directions are the same.

$$G^C = G_n^C + \left(G_s^C - G_n^C\right)\left\{\frac{G_s + G_t}{G_n + G_s + G_t}\right\}^{\eta} \tag{20}$$

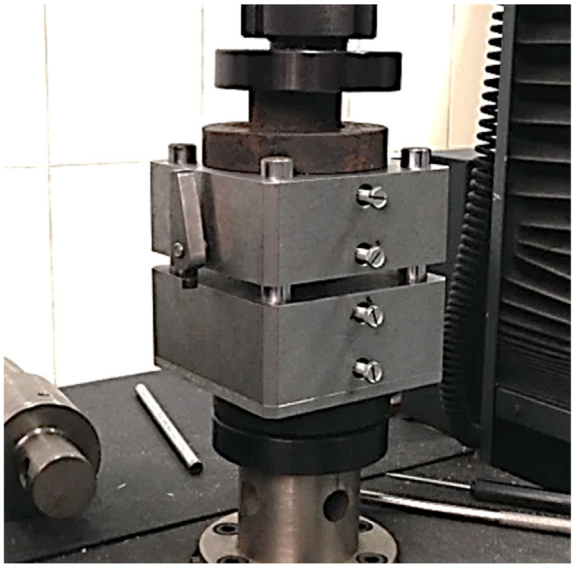

(a) Set-up Photo

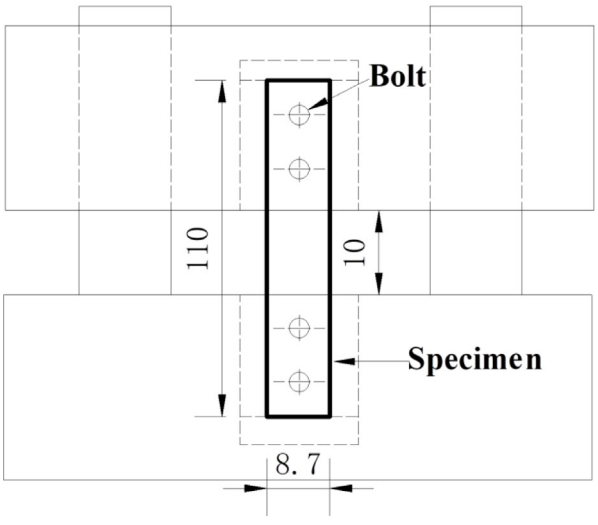

(b) Schematic of experimental set-up

Fig. 6. Compressive specimen (mm).

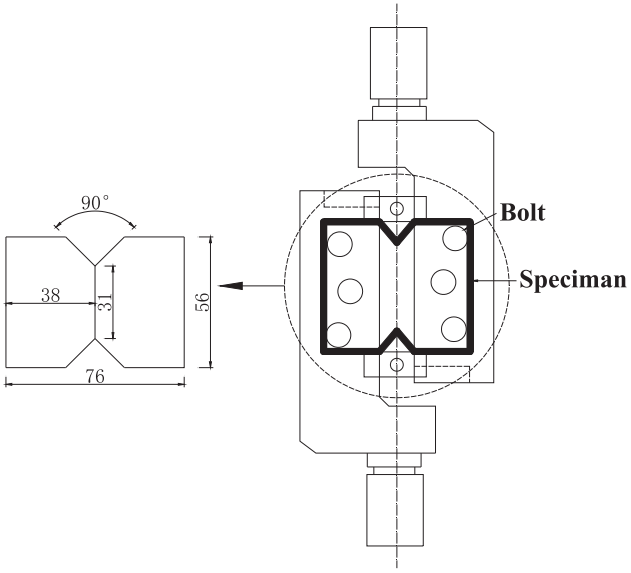

Fig. 7. In-plane shear specimen (mm).

Table 5
Summary of test results.

Property	Number	Elastic Modulus (GPa)				Ultimate Strength (MPa)			
		SD	E_{av}	$E_{95\%}$	*COV*	*SD*	U_{av}	$U_{95\%}$	*COV*
Longitudinal Tensile	5	3.10	47.17	43.12	0.07	33.93	1146.03	1104.50	0.03
Transverse Tensile	5	1.35	16.18	14.51	0.08	5.31	47.45	40.86	0.11
Longitudinal Compressive	5	0.96	55.02	53.82	0.07	70.83	1014.34	926.40	0.02
Transverse Compressive	5	0.06	16.74	15.45	0.06	3.49	168.40	164.20	0.02
In-plane Shear	5	0.46	5.04	4.55	0.09	8.47	48.50	39.38	0.10
Poisson's ratio	5	Longitudinal Poisson's ratio				Transverse Poisson's ratio			
		SD	v_{xyav}	$v_{xy95\%}$	COV	SD	v_{yxav}	$v_{yx95\%}$	COV
		0.017	0.265	0.286	0.06	0.011	0.114	0.128	0.10

Table 6
Summary of resistance factors.

Property	95% Reliability		99% Reliability	
	Elastic Modulus	Ultimate Strength	Elastic Modulus	Ultimate Strength
Longitudinal Tensile	0.88	0.95	0.84	0.93
Transverse Tensile	0.87	0.82	0.81	0.74
Longitudinal Compressive	0.88	0.97	0.84	0.95
Transverse Compressive	0.90	0.97	0.86	0.95
In-plane Shear	0.85	0.84	0.79	0.77
Longitudinal Poisson's ratio	0.90	–	0.86	–
Transverse Poisson's ratio	0.84	–	0.77	–

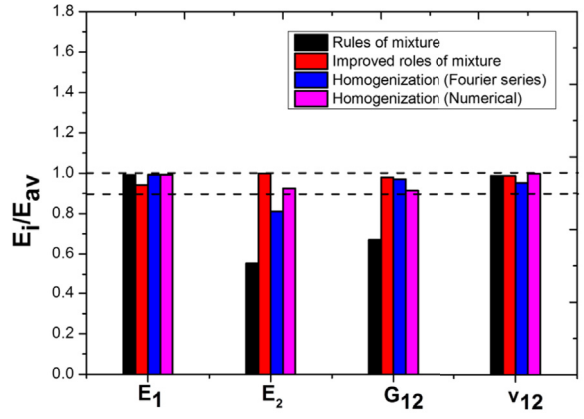

(a) Predicted value to average test results

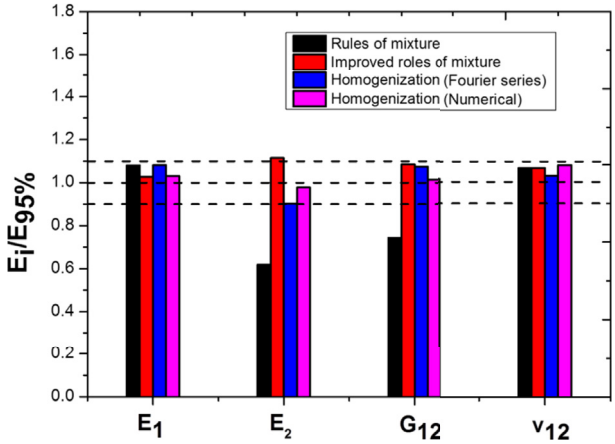

(b) Predicted value to test results with 95% insurance

Fig. 8. Engineering constants comparison.

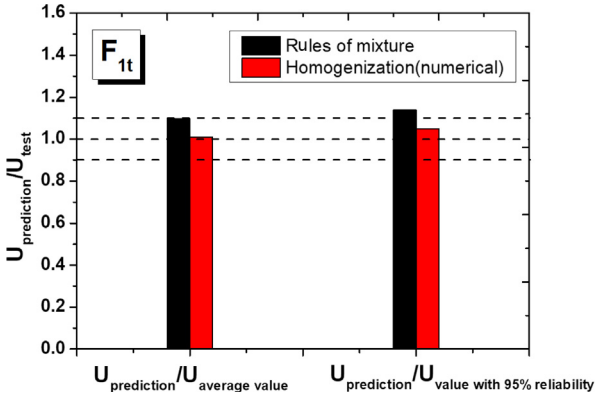

(a) Ultimate strength comparisons

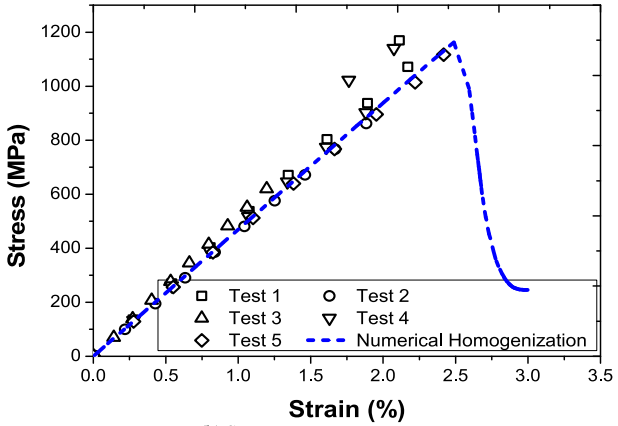

(b) Stress-strain curve comparisons

Fig. 9. Longitudinal tensile behavior comparison.

where: G_n, G_s, and G_t are the corresponding energy release rates under pure modes *I*, *II*, and *III*, the additional subscript "C" denotes critical case, which can be determined based on a standard fracture toughness test and η is a material parameter.

4. Experimental programs and results

4.1. Properties of fiber and resin

Tables 2 and 3 present a summary of the mechanical properties of both E-glass fibers and epoxy resin, respectively [37].

4.2. Processing method

As shown in Fig. 4, a typical pultrusion production line mainly consists of the following components [38]: (i) roving/fabric stacked on creels, (ii) pre-forming guide plate, (iii) resin impregnator, (iv) forming & curing die, and (v) a pulling system and cutting system. E-glass rovings with the type of 9600 TEX are employed. Glass fibers rovings are guided by a pre-forming plate from a creel into a resin impregnation tank for wetting the reinforcements with the polymeric matrix. The pre-forming guide plate guides positions of reinforcements in the designed locations in the cross section of profiles. The wetted reinforcements are then traveled through the heated die to cure epoxy resin drawn by pulling system. The resin matrix progressively changes from liquid to gel and finally to solid. After performing and shaping, the composites are pulled out and cut off based on the required length.

4.3. Density & fiber volume fraction tests

In this study, three specimens with nominal dimensions of 25.0 mm × 25.0 mm × 4.0 mm were fabricated to investigate the fiber fraction based on calcination methods [39] and density [40]. The specimens were weighed to acquire composite destiny before burning in an incinerator. After burning, the remaining consists only of fiber that was weighed to determine the fiber volume fraction of each specimen. Table 4 presents a summary of the results of these tests. As shown in this table, the average density of the pultruded composite lamina is 1920.10 kg/m^3 with an average fiber volume fraction of 56.2%.

4.4. Test specimens

The tensile performance, Poisson's ratio, compressive performance, and in-plane shear performance of pultruded lamina have been experimentally investigated. As shown in Fig. 5, five specimens were tested under tension load parallel to fiber direction and five specimens were tested under tension load perpendicular to fiber direction in order to measure the ultimate tensile strength, elastic modulus and the Poisson's ratio based on procedures described in reference [41]. The typical dimensions of the longitudinal tensile specimens are 230.0 mm × 15.00 × 4.0 mm, while the

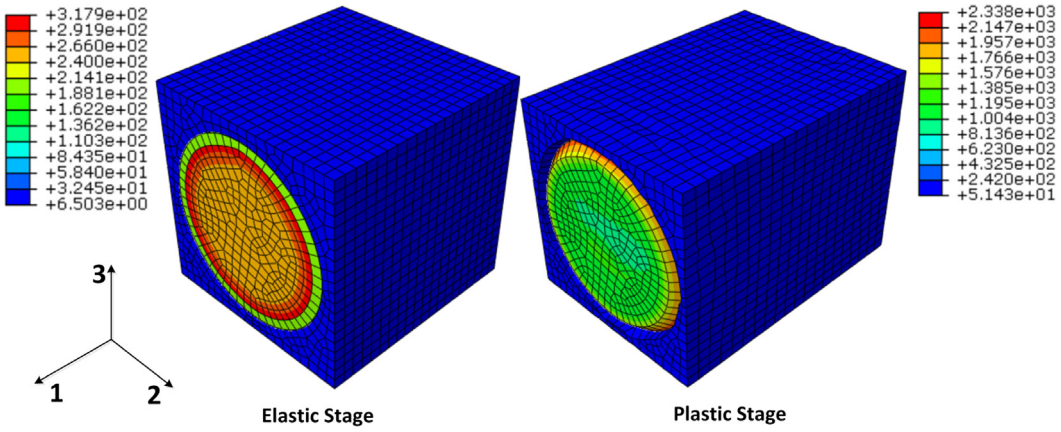

(a) Mises stress

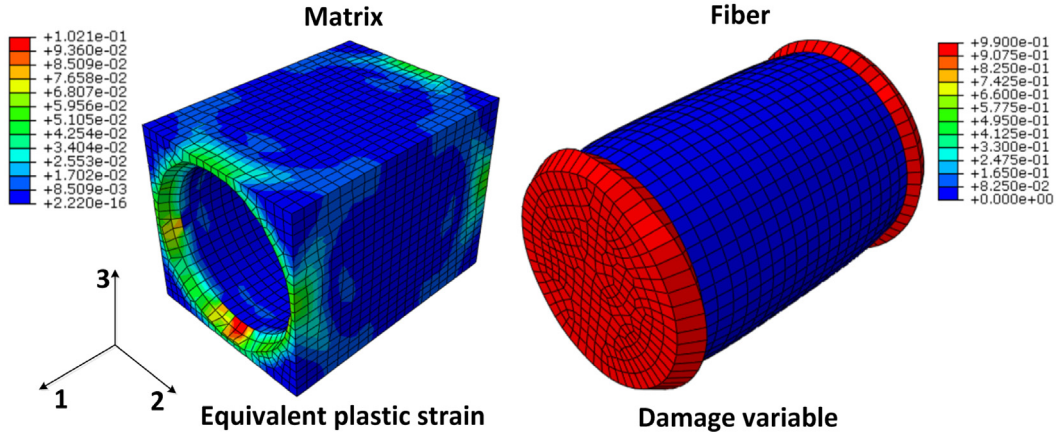

(b) Equivalent plastic strain and damage variable

Fig. 10. Stress, plastic strain and damage distributions of the unit cell under longitudinal tensile loading (*11*-direction).

dimensions of the transverse tensile specimens are 170.0 mm × 25.0 mm × 4.0 mm. In addition, five specimens were tested under compression along the fiber direction and another five specimens perpendiculars to the fiber direction [42] were also tested under compression (refer to Fig. 6). The average dimension of the compressive specimens is 110.0 mm × 8.7.0 mm × 4.0 mm with an effective compressive length of 10.0 mm. A total of five specimens were also prepared based on procedures described in reference [43] to measure the in-plane shear strength and modulus of each specimen (refer to Fig. 7). The average dimension of the in-plane shear specimen is 76.0 mm X 56.0 mm X 4.0 mm (see Fig. 7). The loads and displacements were measured by a calibrated universal testing machine (UTM) load cell and displacement sensor, respectively, while strains were measured using electrical strain gauges during the loading process.

4.5. Experimental results

Table 5 presents a summary of the experimental results. In this table, *SD* is the standard deviation, *COV* is the coefficient of variability, E_{av} is the average elastic modulus, $E_{95\%}$ is the elastic modulus with 95% reliability, U_{av} is the average ultimate strength, and $U_{95\%}$ is the ultimate strength with 95% reliability.

The average longitudinal tensile strength, transverse tensile strength, longitudinal compressive stress, transverse compressive stress, and the in-plane shear stresses obtained from the tests are 1146.03 MPa, 47.45 MPa, 1014.34 MPa, 168.40 MPa and 48.50 MPa, respectively. The average experimental values of longitudinal tensile elastic modulus, transverse tensile elastic modulus, longitudinal compressive elastic modulus, transverse compressive elastic modulus and in-plane shear modulus are 47.17 GPa, 16.18 GPa, 55.02 GPa, 16.74 GPa and 5.04 GPa, respectively. Experimental results also indicated that the average longitudinal and transverse Poisson's ratio are 0.265 and 0.114, respectively. Test results showed that the experimental value of the in-plane shear strength is smaller than the predicted value obtained in previous studies [12–14]. This variation may be attributed to the fact that the behavior of woven reinforced lamina is different from unidirectional GFRP lamina.

4.6. Resistance factor

The load and resistance factor design (LRFD) protocol is commonly adopted in the design of structures. According to LRFD design method, the resistance of the structure and the applied loads are considered separately. The design should satisfy the following inequality [44].

$$\Phi F > \alpha_D L_D + \psi \sum_{j=1}^{N_L} \alpha_j L_j \tag{21}$$

where: F is material strength, Φ is resistance factor, α_D is dead load factor, L_D is dead load, α_j is live load factors, L_j is other loads including live, pressure, thermal, acceleration etc., and N_L is the number of other types of design loads.

Now, assuming that the applied stress is deterministic, the resistance factor could be obtained for a given reliability relation as follows [15]:

$$\Phi = \frac{\mu_F + z\bar{\omega}_F}{\mu_F} = 1 + zC_F \le 1 \tag{22}$$

where: μ_F is average strength, $\bar{\omega}_F$ is standard deviation (SD), C_F is the coefficient of variability (COV), z is variable in terms of standard normal Gaussian probability density function.

The results of the resistance factors are summarized in Table 6. If the required reliability is 95%, the resistance factor of the elastic modulus will then falls between 0.84 and 0.90, and the corresponding ultimate strength resistance factor will fall in the range of 0.82–0.97. In case that the required reliability is 99%, the elastic modulus resistance factor will fall between 0.77 and 0.86 while the ultimate strength resistance factor falls within a range between 0.74 and 0.95. Therefore, the minimum resistance factor is adopted on the safety side, where an ultimate strength resistance factor is 0.8 for 95% reliability and 0.7 for 99%.

5. Comparisons and discussion

5.1. Engineering constants comparisons

Using Eq. (A.1.1) of Appendix A, the predicted density of composites is 1946.8 kg/m^3, and the difference between theoretical value and experimental value is within 3%.

Fig. 8, shows a comparison between analytical, numerical, and experimental engineering constants results. It is noted that all the predicted values of both the longitudinal elastic modulus E_1 and longitudinal Poisson's ratio, v_{12}, agreed well with the average experimental results and that the test results fall within 95% reliability, with a difference of about 10%. For the transverse elastic modulus, E_2, the predicted value obtained from the *improved* rules-of-mixture approach and numerical homogenization agreed well with the average values of the experimental results where test results fall within a 95% reliability. However, predicted values obtained from other methods tended to be smaller than the average

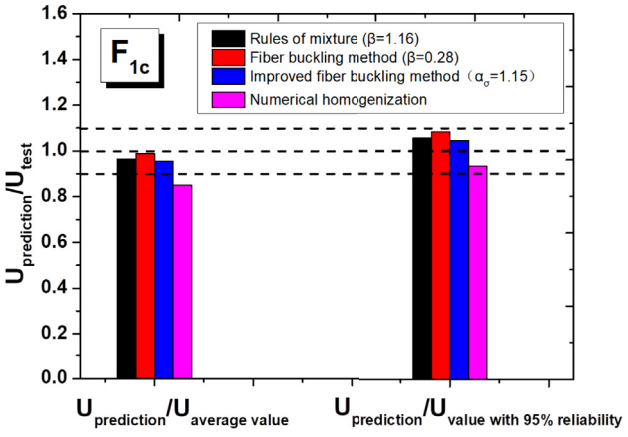

(a) Ultimate strength comparisons

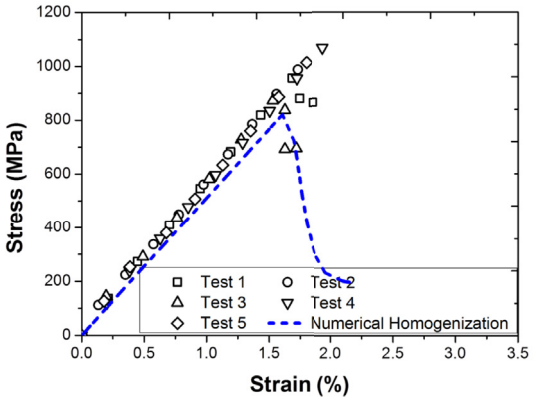

(b) Stress-strain curve comparisons

Fig. 11. Longitudinal compressive behavior comparison.

test results. With respect to the in-plane shear modulus, the predicted value, except of the case of rules of mixture, agreed well with both the average experimental results that test results fall within 95% reliability.

5.2. Ultimate strength comparisons

5.2.1. Longitudinal tensile strength

Fig. 9 shows comparisons between experimental and theoretical ultimate strength and stress-strain relationship for specimens subjected to longitudinal tensile loading. As shown in Fig. 9-a, the predicted ultimate strength values obtained from the "rules of mixture" equations (Eq. B.1.1 in Appendix B), and the "numerical homogenization" approach both agreed well with experimental results. As shown in this figure, the predicted value obtained from the "rules of mixture" approach is 10% larger than the average experimental results but is about 14% larger than the experimental results with 95% reliability. In addition, the difference between predicted results obtained from "numerical homogenization" approach and corresponding experimental results is within 7%. Also, theoretical stress-strain relationship for specimens subjected to longitudinal tensile loading calculated using "numerical homogenization" agreed well with experimental values (refer to Fig. 9-b).

Fig. 10 presents the Mises stress, equivalent plastic strain, and the damage distributions in the unit cell domain under longitudinal tensile loading. As shown in Fig. 10-a, in the elastic stage, the fibers Mises stress are generally much larger than the matrix stresses due to elastic moduli of fiber is larger than the matrix. One can also see that the plastic strains developed gradually in the matrix phase and that fiber-matrix de-bonding developed gradually as load along fiber direction increased. The Mises stress has a periodic distribution in both the elastic and plastic stages under longitudinal tensile loading, indicating that the unit cell was modeled with correct periodic boundary conditions based on Eqs. (7) and (8). As shown in Fig. 10-b, the load is applied along fiber direction reached its maximum value when the fiber damage initiated, and this failure agreed well with the basic assumption of the *role of mixtures* approach presented in Eq. B.1.1 in Appendix B.

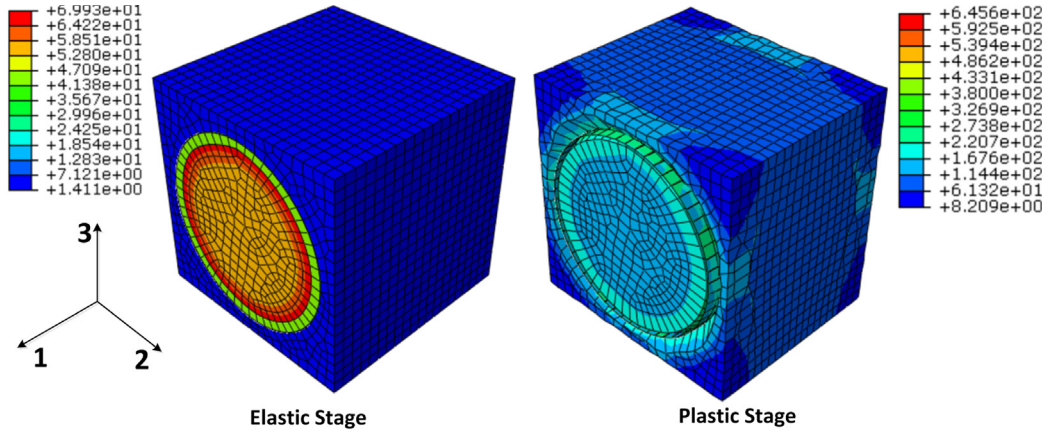

(a) Mises stress

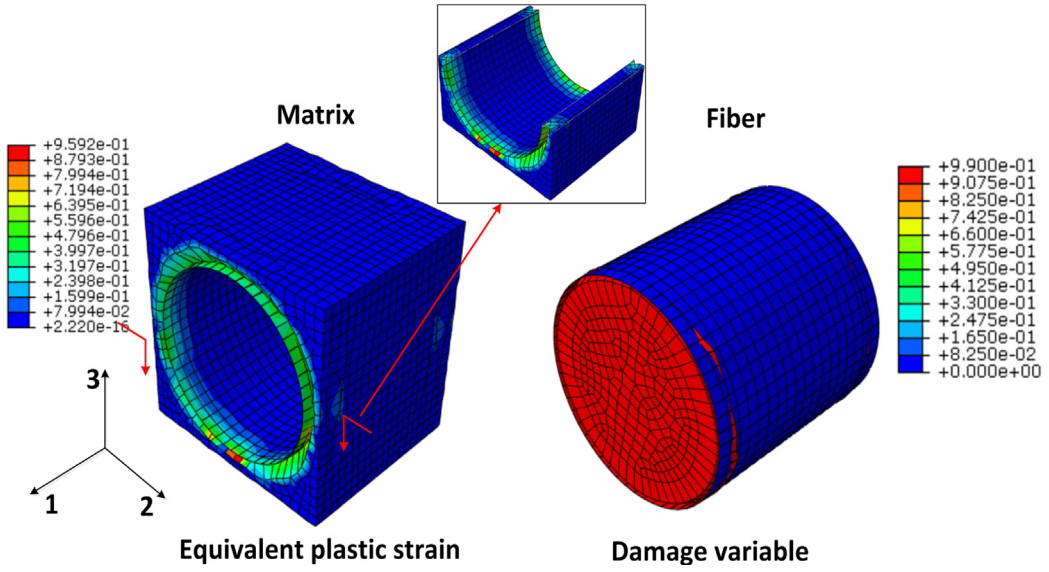

(b) Equivalent plastic strain and damage variable

Fig. 12. Stress, plastic strain and damage distributions of unit cell under longitudinal compressive loading (*11*-direction).

5.2.2. Longitudinal compressive strength

Fig. 11 presents comparisons between theoretical and experimental ultimate strength and stress-strain relationships for specimens subjected to longitudinal compressive loads. Assuming a value of 1.16 for the correction factor, β, in the "rules of mixture" equation (Eq. B.2.1 in Appendix B), results in differences between predicted and experimental results within 10%. On the other hand, if one assumes that the correction factor, β, is equal to 0.28 in the "fiber buckling method" (Eq. B.2.2 in Appendix B), the predicted value would agree well with test results. The predicted result of the "improved fiber buckling method" (Eq. B.2.3 in Appendix B) agrees well with experimental results if a fiber misalignment standard deviation of $\alpha_\sigma = 1.15$ is assumed. Also, results showed that the predicted value obtained from the "numerical homogenization" approach is 14% less than the average experimental results and 6% less than the experimental results with 95% reliability. As shown in Fig. 11-b, the predicted stress-strain relationship based on "numerical homogenization" method generally agrees well with test results.

Fig. 12 presented Mises stress, equivalent plastic strain, and damage distributions in the unit cell domain under longitudinal compressive loading. As is shown in Fig. 12-a, in the elastic stage, the elastic modulus of fiber is much larger than the matrix leading to that fiber distributed larger Mises stress. The Mises stress of both fiber and matrix presented periodic distribution in both the elastic stage and plastic stage. Obvious plastic strain appeared in the matrix phase and fiber-matrix de-bonding occurred in the plastic stage. As is shown in Fig. 12-b, de-bonding between fiber and matrix interface and damage of fiber led to final failure under longitudinal compressive loading.

5.2.3. Transverse tensile strength

Fig. 13 presents the ultimate strength and stress-strain relationship comparisons under transverse tensile loading. The predicted value obtained from the stress concentration method in Eq. B.3.1 of Appendix B, with concentration factor proposed by Agarwal [18] (Eq. B.3.2 in Appendix B) is less than experimental results, while the difference between the predicted value from the stress concentration method with the concentration factor proposed by Huang [20] (Eq. B.3.3 in Appendix B) falls within 10% under assuming bridge factor β as 0.70. The predicted value based on linear fracture mechanics method (Eq. B.3.6 in Appendix B) agreed well with test results if mode I critical fracture energy G_{1c} is assumed to be 140.0 J/m^2. Now, assuming V_v to be 0.02, based on Ref. [15], the predicted value using the empirical equation is 5% larger than the average test results and 20% larger than the test results with 95% reliability. The predicted value from the "numerical homogenization" method is 1.5% less than the average experimental results and 10.5% less than the experimental results with 95% reliability. As is shown in Fig. 13-b, the stress-strain relationship predicted from the "numerical homogenization" method for specimens subjected to transverse tensile loading agreed well with test values.

Fig. 14 presents Mises stress, equivalent plastic strain and damage distributions in the unit cell domain under transverse tensile loading. As shown in Fig. 14-a, the Mises stress for both the fibers and the matrix exhibited periodic distribution in both the elastic stage and plastic stage. The maximum Mises stress value in the elastic stage appeared in the middle of fibers, while the maximum Mises stress in the plastic stage occurred near the interface. As shown in Fig. 14-b, de-bonding between fiber and matrix interface and damage of matrix led to final failure under transverse tensile loading. No fiber damage occurred during the transverse tensile

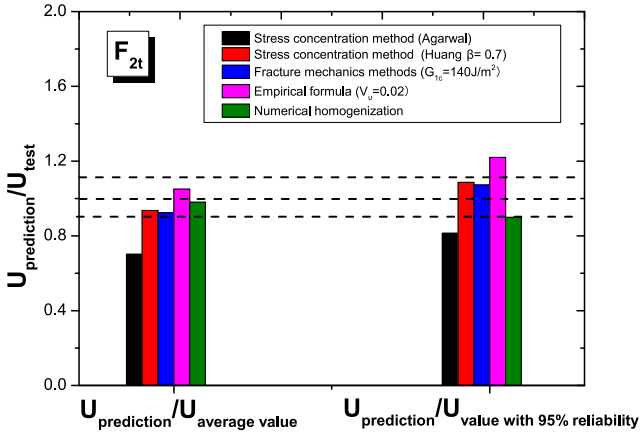

(a) Ultimate strength comparisons

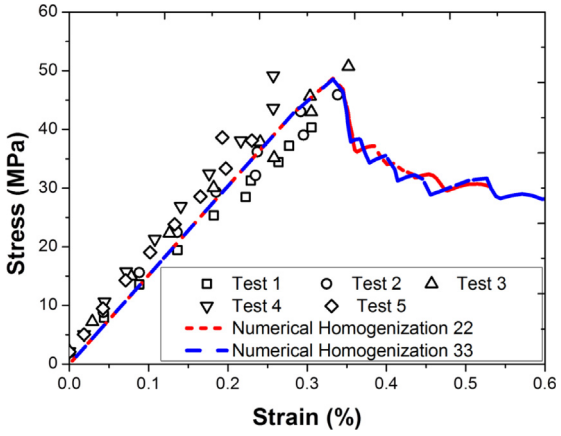

(b) Stress-strain curve comparisons

Fig. 13. Transverse tensile behavior comparison.

loading, indicating that the transverse tensile behavior is mainly controlled by matrix and interface performance.

5.2.4. Transverse compressive strength

Fig. 15 presents comparisons between theoretical and experimental values of both the ultimate strength and stress-strain relationship for specimens subjected to transverse compressive loading. The predicted value from the "*strain amplification method*" (Eq. B.4.1 in Appendix B) is 10% larger than the average experimental value and is 12.5% larger than the test value with 95% reliability. However, the predicted result based on the empirical formula described in Eq. B.4.2 of Appendix B is much less than the experimental results. On the other hand, the predicted value from the "numerical homogenization" method is 2.5% larger than the average experimental results, and 5.5% larger than the experimental results with 95% reliability. As shown in Fig. 15-b, the stress-strain relationship obtained from the "numerical homogenization" for specimens subjected to transverse compressive loading agreed well with test values.

Fig. 16 presents the Mises stress, equivalent plastic strain, and damage distributions in the unit cell domain under transverse compressive loading. As is shown in Fig. 16-a, the Mises stress of both fibers and matrix exhibited periodic distribution and that the maximum Mises stress appeared in the middle of fiber in both elastic stage and plastic stage. Also, Fig. 16-b shows that the damage of matrix led to the final failure under transverse compressive

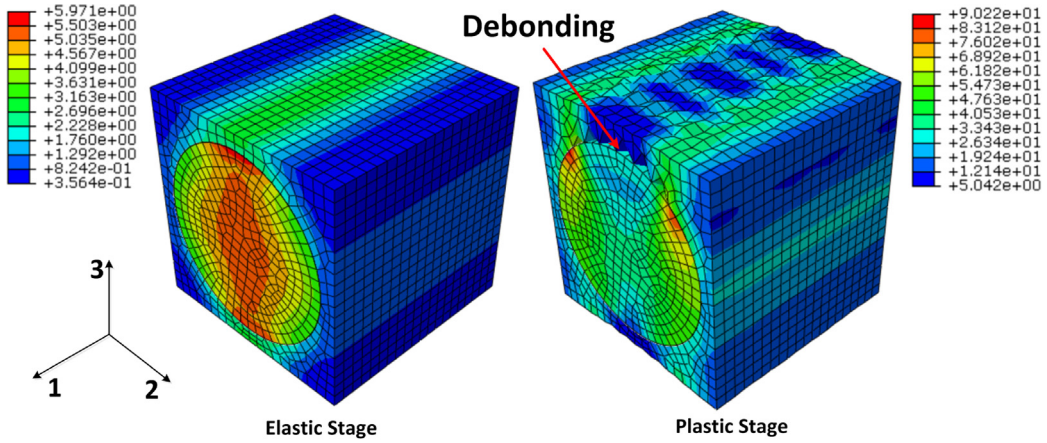

(a) Mises stress

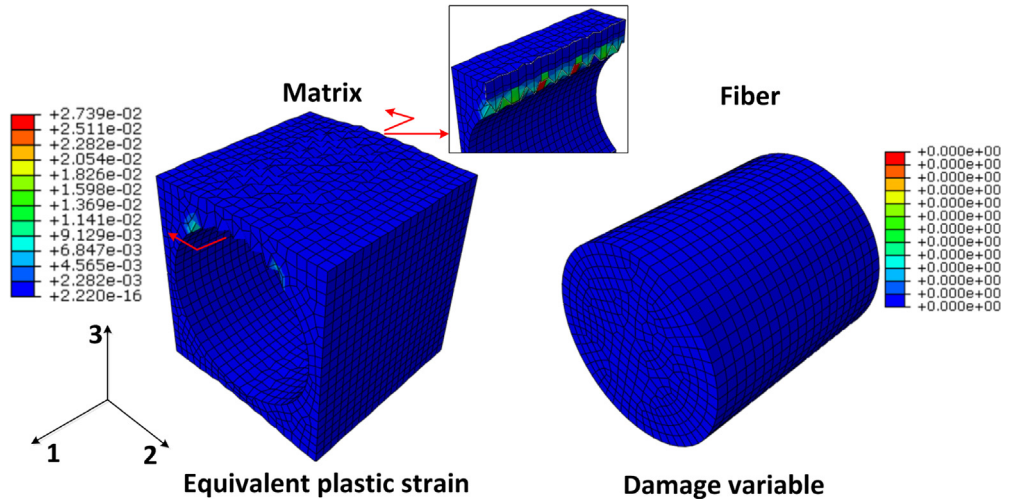

(b) Equivalent plastic strain and damage variable

Fig. 14. Stress, plastic strain and damage distributions of unit cell under transverse tensile loading (33-direction).

loading. Again, no fiber damage occurred during the transverse compressive loading, indicating that the transverse compressive behavior is mainly controlled by matrix plasticity.

5.2.5. Ultimate shear strength

Fig. 17 presents comparisons between the theoretical and experimental ultimate strength and stress-strain relationship for specimens subjected to in-plane shear loads. As shown in the figure, the analytical results obtained from the "fracture mechanics" methods is 1% less than the average corresponding experimental value, and is 12.5% larger than the test value, with 95% reliability under the assumption that the mode *II* critical fracture energy, G_{2c}, is 220 J/m^2. Also, the predicted value from the "numerical homogenization" approach is 1.2% larger than the average experimental results and is 18.5% larger than the experimental results with 95% reliability.

Fig. 18 presents the Mises stresses, the equivalent plastic strain, and the damage distributions in the unit cell domain for specimens subjected to in-plane shear loads. As shown in Fig. 18-a, the maximum Mises stress appeared periodically at both the top and the bottom middle surface in the elastic stage. The stress redistributed due to material damage, and the maximum Mises stress occurred in the fiber due to matrix damage. As shown in Fig. 18-b, debonding between fiber and matrix interface and matrix damage led to the final failure of specimens subjected to in-plane shear loads. Again, no fiber damage was observed during in-plane shear loading, indicating that the in-plane shear behavior is mainly controlled by matrix and interface performance.

Due to the fact that the thickness of the FRP plate is relatively small, it is usually difficult to experimentally define the transverse shear behavior of composites. For this reason, the numerical homogenization approach may provide a satisfactory reference for the transverse shear behavior of unidirectional FRP materials. Fig. 19 show the numerical shear stress-strain curves. As shown in Fig. 19, one can notice a difference between the in-plane shear modulus and the transverse shear modulus (*23*-direction), while only a small difference is observed between the transverse shear strength (*23*-direction) and the in-plane shear strength (*13*-direction). It is commonly accepted that in case of lack of sufficient material test data, transverse shear strength of a pultruded unidirectional GFRP lamina could be assumed to be the same as its in-plane shear strength value [14]. The Mises stress, the equivalent plastic strain, and the damage distributions in the unit cell domain under transverse shear loading are presented in Fig. 20. As shown in Fig. 20-a, the maximum Mises stress periodically appeared in the fibers near the matrix-fiber interface in both elastic and plastic

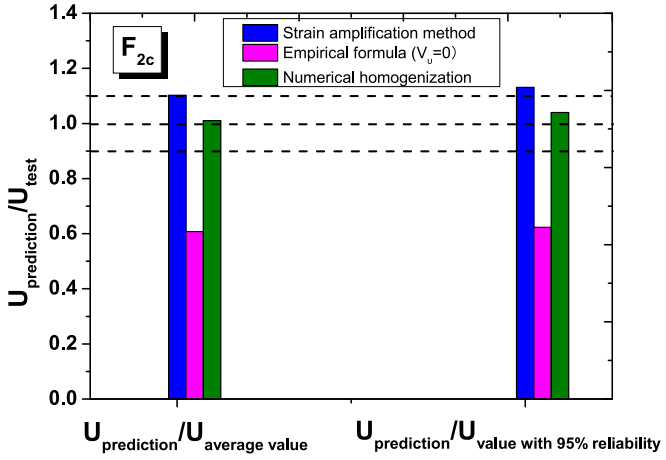

(a) Ultimate strength comparisons

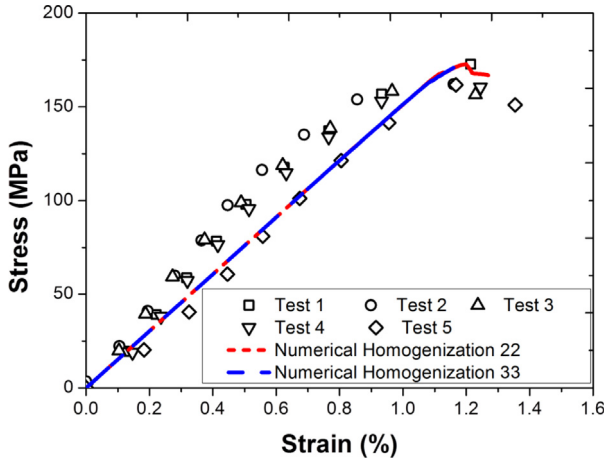

(b) Stress-strain curve comparisons

Fig. 15. Transverse compressive behavior comparison.

stage. As shown in Fig. 20-b, damage of the matrix led to the final failure under transverse shear loading. No fiber damage occurred during in-plane shear loading, indicating that the transverse shear behavior is mainly controlled by matrix performance.

6. Conclusions

Analytical and numerical homogenization methods were successfully used in this study to effectively model the macroscopic properties of unidirectional GFRP pultruded composite lamina. Five identical specimens were experimentally evaluated under tensile, compressive and shear loads in order to validate the proposed theoretical and numerical results. Based on the results of this study, the following conclusions are drawn:

- Results of this study indicated that numerical homogenization approach is shown to be effective for accurate prediction of the non-linear behavior pultruded composites. The differences between numerical homogenization and the average experimental results of longitudinal tensile, transverse tensile, transverse compression and in-plane shear fall within a 5% range. However, numerical homogenization results related to compressive strength is 14% less than the average experimental results. In general, a good correlation between numerical homogenization results and test results is achieved.
- The damage of unidirectional GFRP lamina subjected to longitudinal tensile and compressive loads is controlled mainly by the extent of fiber damage, while transverse tensile and compressive stresses, in-plane and shear behaviors of the unidirectional GFRP lamina are controlled by both matrix and fiber-matrix interface damages. It should be noted that in order to accurately predict different failure modes, numerical results should be verified by conducting micro-scale experimental tests of the GFRP lamina.

Conflict of interests

The authors indicated that there are no conflicts of interests.

Acknowledgment

The authors gratefully acknowledge the financial support provided by National Natural Science Foundation [Grant # 51578406 and #51808398] of People's Republic of China.

Appendix A. Prediction of engineering constants

The engineering constants of a unidirectional lamina include longitudinal elastic modulus E_1, transverse elastic modulus E_2, in-plane shear modulus G_{12}, transverse shear modulus G_{23}, longitudinal Poisson's ratio ν_{12} and transverse Poisson's ratio ν_{23}.

A.1. Rules of mixtures

All engineering constants could be approximated based on rules-of-mixtures [19] as follows:

$$\rho_c = \rho_f V_f + \rho_m V_m \quad \text{A.1.1}$$

$$E_1 = E_{f1} V_f + E_m V_m \quad \text{A.1.2}$$

$$E_2 = \frac{E_{f2} E_m}{E_m V_f + E_{f2} V_m} \quad \text{A.1.3}$$

$$G_{12} = \frac{G_{f12} G_m}{G_m V_f + G_{f12} V_m} \quad \text{A.1.4}$$

$$\upsilon_{12} = \upsilon_f V_f + \upsilon_m V_m \quad \text{A.1.5}$$

where: ρ_f *is* the density of fiber, ρ_m is the density of resin, E_{f1} *is* the longitudinal elastic modulus of fiber, E_{f2} *is* the transverse elastic modulus of fiber, V_f is the fiber volume fraction, υ_f is Poisson's ratio of fiber, E_m is the elastic modulus of matrix, V_m is resin volume fraction, υ_m is Poisson's ratio of resin. G_f is the shear modulus of fiber, G_m is the shear modulus of resin.

A.2. Improved rules of mixtures

To account for initial imperfections, the formulations of rules-of-mixture were improved as following [16]:

$$E_1 = E_{f1} V_f + \eta_1 E_m V_m \quad \text{A.2.1}$$

$$E_2 = E_3 = \frac{E_{f_2} E_m [V_f + \eta_2 V_m]}{E_m V_f + E_{f_2} \eta_2 V_m} \quad \text{A.2.2}$$

$$\eta_2 = \frac{0.2}{1 - \upsilon_m} \left(1.1 - \sqrt{\frac{E_m}{E_f}} + \frac{3.5 E_m}{E_f} \right) (1 + 0.22 V_f) \quad \text{A.2.3}$$

$$G_{12} = G_{13} = \frac{G_f G_m [V_f + \eta_{12} V_m]}{G_m V_f + G_f \eta_{12} V_m} \quad \text{A.2.4}$$

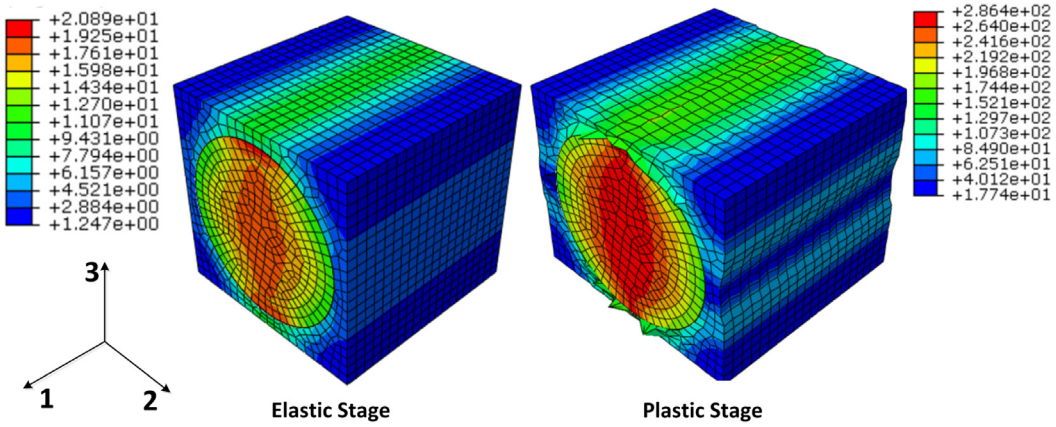

(a) Mises stress

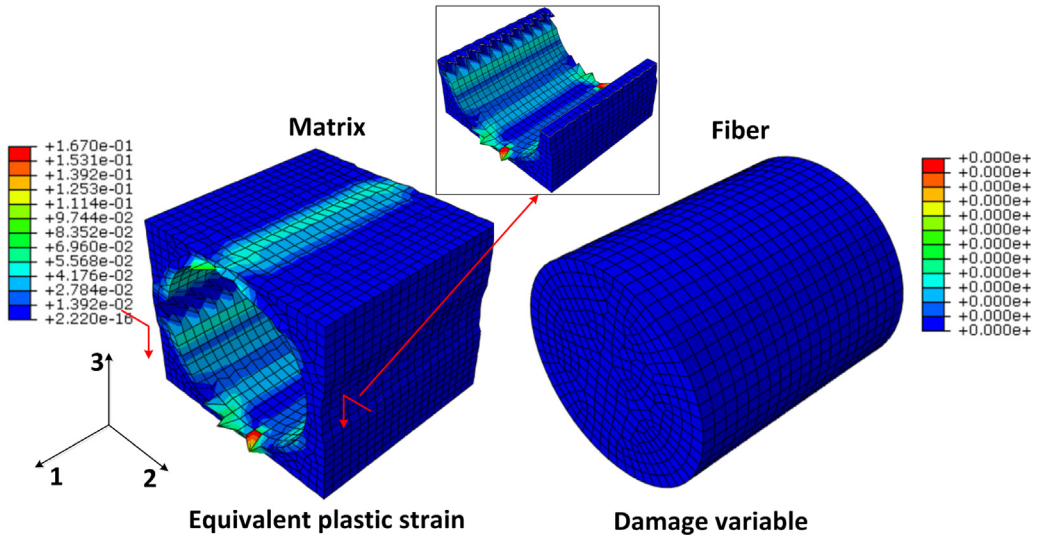

(b) Equivalent plastic strain and damage variable

Fig. 16. Stress, plastic strain and damage distributions of unit cell under transverse compressive loading (33-direction).

$$\eta_{12} = 0.28 + \sqrt{\frac{E_m}{E_f}} \quad \text{A.2.5}$$

$$G_{23} = \frac{G_f G_m [V_f + \eta_{23} V_m]}{G_m G_f + G_f \eta_{23} V_m} \quad \text{A.2.6}$$

$$\eta_{23} = 0.388 - 0.665\sqrt{\frac{E_m}{E_f}} + 2.56\frac{E_m}{E_f} \quad \text{A.2.7}$$

$$v_{23} = k(v_f V_f + v_m V_m) \quad \text{A.2.8}$$

$$k = 1.095 + 0.27(0.8 - V_f) \quad \text{A.2.9}$$

A.3. Analytical homogenization method

The lamina's engineering constants could be explicitly obtained in terms of the coefficients of the stiffness tensor [17,45].

$$E_1 = C_{11}^* - \frac{2C_{12}^{*2}}{C_{22}^* + C_{33}^*} \quad \text{A.3.1}$$

$$E_2 = \frac{(2C_{11}^* C_{22}^* + 2C_{11}^* C_{23}^* - 4C_{12}^{*2})(C_{22}^* - C_{23}^* + 2C_{44}^*)}{3C_{11}^* C_{22}^* + C_{11}^* C_{23}^* + 2C_{11}^* C_{44}^* - 4C_{12}^{*2}} \quad \text{A.3.2}$$

$$G_{12} = G_{13} = C_{66}^* \quad \text{A.3.3}$$

$$v_{12} = v_{13} = \frac{C_{12}^*}{C_{22}^* + C_{23}^*} \quad \text{A.3.4}$$

$$v_{23} = \frac{C_{11}^* C_{22}^* + 3C_{11}^* C_{23}^* - 2C_{11}^* C_{44}^* - 4C_{12}^{*2}}{3C_{11}^* C_{22}^* + C_{11}^* C_{23}^* + 2C_{11}^* C_{44}^* - 4C_{12}^{*2}} \quad \text{A.3.5}$$

$$G_{23} = \frac{C_{22}^*}{4} - \frac{C_{23}^*}{4} + \frac{C_{44}^*}{2} = \frac{E_2}{2(1 + v_{23})} \quad \text{A.3.6}$$

where: C_{ij}^* (i = 1…3, j = 1…3) is coefficients of the stiffness tensor. It is assumed that the composite has periodic microstructure in a square array and that the Fourier series could be used to estimate all the components of stiffness tensor. In terms of square symmetrical microstructure, the stiffness tensor has six unique coefficients and details are given in [17].

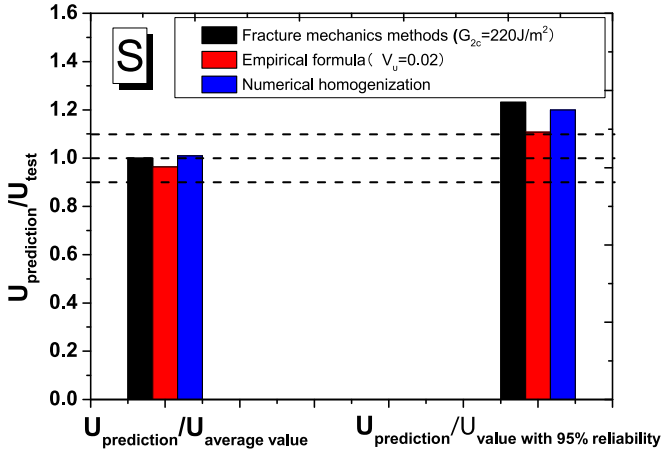

(a) Ultimate strength comparisons

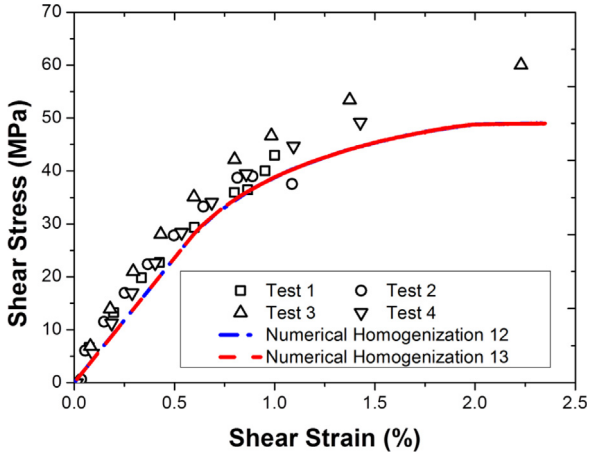

(b) Stress-strain curve comparisons

Fig. 17. In-plane shear behavior comparison.

Appendix B. Prediction of ultimate strength

B.1. Ultimate longitudinal tensile strength

By assuming that all the fibers have the same tensile strength, both the fibers and the matrix behave linearly up to failure, the fibers are brittle with respect to the matrix and the fibers are stiffer than the matrix, the longitudinal tensile strength is controlled by the fiber strength and represented as follows based on rules-of-mixtures. [15,18,19]

$$F_{1t} = F_{ft}\left(V_f + \frac{E_m}{E_f}V_m\right) \tag{B.1.1}$$

where: F_{ft} is the fiber tensile strength.

B.2. Ultimate longitudinal compressive strength

B.2.1. Rules of mixtures

Based on the assumption of *rules of mixtures*, the longitudinal compressive strength could simply be predicted as the smaller value obtained from Eq. B.2.1 [15].

$$F_{1c} = \begin{cases} F_{fc}[\beta V_f + V_m \frac{E_m}{E_f}] \\ F_{mc}[V_m + \beta V_f \frac{E_m}{E_f}] \end{cases} \tag{B.2.1}$$

where: β is a correction coefficient for longitudinal compressive strength, F_{fc} is the compressive strength of fibers, F_{mc} is the matrix compressive strength.

B.2.2. Fiber buckling method

The longitudinal compressive failure mode is assumed to be triggered by fiber micro-buckling when individual fibers buckle within the matrix. In this case, the longitudinal compressive strength is considered to be the smaller value of in-phase shear mode and out-of-phase mode [15,18].

$$F_{1c} = \begin{cases} 2V_f\sqrt{\frac{\beta E_f E_m V_f}{3V_m}} & In-phase\ shear\ mode \\ \frac{\beta G_m}{1-V_f} & out-of-phase\ mode \end{cases} \tag{B.2.2}$$

B.2.3. Improved fiber buckling method

The fiber buckling method is improved to account for fiber misalignment and expressed as follows [15]:

$$F_{1c} = G_{12}\left(1 + \frac{4.76G_{12}\alpha_\sigma}{S}\right)^{-0.69} \tag{B.2.3}$$

where: α_σ is the standard deviation of fiber misalignment.

B.3. Ultimate transverse tensile strength

B.3.1. Strength concentration method

It is assumed that the transverse strength of composites is controlled by the matrix ultimate strength and is lower than the matrix strength by a factor known as strength concentration factor (*SCF*), which depended on the relative properties of the fibers and the matrix and their volume fractions. Thus, the transverse composite strength could be expressed as [18]:

$$F_{2t} = F_{mt}/SCF \tag{B.3.1}$$

where: F_{mt} is the matrix tensile strength. Agarwal et al. [18] proposed the following expression for determining *SCF*:

$$SCF = \frac{1 - V_f[1 - E_m/E_f]}{1 - (4V_f/\pi)^{1/2}[1 - E_m/E_f]} \tag{B.3.2}$$

Huang [20] also proposed *SCF* formula with transversely isotropic fibers derived upon isotropic fiber reinforcement as:

$$SCF = \left[1 + \frac{\sqrt{V_f}}{2}A' + \frac{\sqrt{V_f}}{2}(3 - V_f - \sqrt{V_f})B'\right] \times \left[\frac{(V_f + \beta V_m)E_{f2} + V_m(1-\beta)E_m}{\beta E_{f2} + (1-\beta)E_m}\right] \tag{B.3.3}$$

$$A' = \frac{[1 - \upsilon_m - 2\upsilon_m^2]E_{f2} - [1 - \upsilon_{f23} - 2\upsilon_{f23}^2]E_m}{E_{f2}(1 + \upsilon_m) + E_m\left(1 - \upsilon_{f23} - 2\upsilon_{f23}^2\right)} \tag{B.3.4}$$

$$B' = \frac{E_m(1 + \upsilon_{f23}) - E_{f2}(1 + \upsilon_m)}{E_{f2}(-3 + \upsilon_m + 4\upsilon_m^2) - E_m(1 + \upsilon_{f23})} \tag{B.3.5}$$

where: β is bridging parameter.

B.3.2. Fracture mechanic method

It is assumed that the transverse tensile failure of a unidirectional lamina occurs when a transverse crack propagates along the fiber direction [15], the transverse tensile strength could be obtained as follows:

$$F_{2t} = \sqrt{\frac{G_{1c}}{1.12^2\pi(t_t/4)\Lambda_{22}^0}} \tag{B.3.6}$$

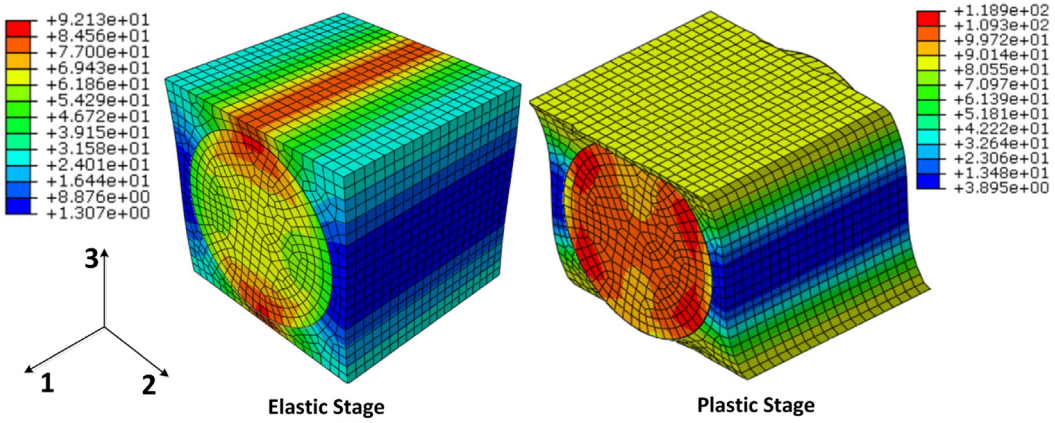

(a) Mises stress

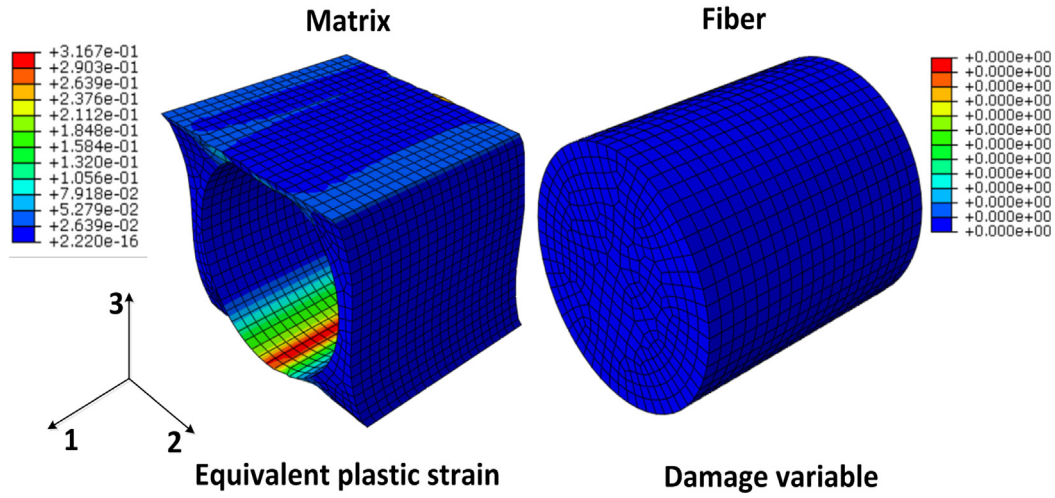

(b) Equivalent plastic strain and damage variable

Fig. 18. Stress, plastic strain and damage distributions of the unit cell under in-plane shear loading (*13*-direction).

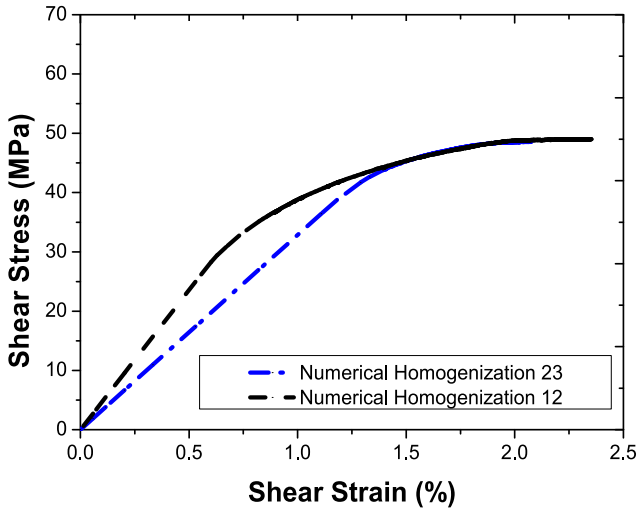

Fig. 19. Stress-strain curve of transverse shear.

$$\Lambda_{22}^{0} = 2\left(\frac{1}{E_2} - \frac{v_{12}^2 E_2^2}{E_1^3}\right) \qquad \text{B.3.7}$$

where: G_{1c} is the fracture toughness in mode *I*, t_t is the transition thickness.

B.3.3. Empirical formula

An empirical formula for estimating the transverse tensile strength is adopted [15,23,24].

$$F_{2t} = F_{mt}\left[1 - \sqrt{\frac{4V_v}{\pi(1-V_f)}}\right]\left[1 + \left(V_f - \sqrt{V_f}\right)\left(1 - \frac{E_m}{E_{f2}}\right)\right] \qquad \text{B.3.8}$$

where: V_v is the void volume fraction, F_{mt} is the matrix tensile strength.

B.4. Ultimate transverse compressive strength

B.4.1. Strain amplification method

The transverse compressive strength could be obtained by strain-amplification factor method as follows [21,22]:

$$F_{2c} = E_2\varepsilon_{mc}\left\{1 - (4V_f/\pi)^{1/2}[1 - E_m/E_f]\right\} \qquad \text{B.4.1}$$

where: ε_{mc} is the matrix ultimate compressive strain.

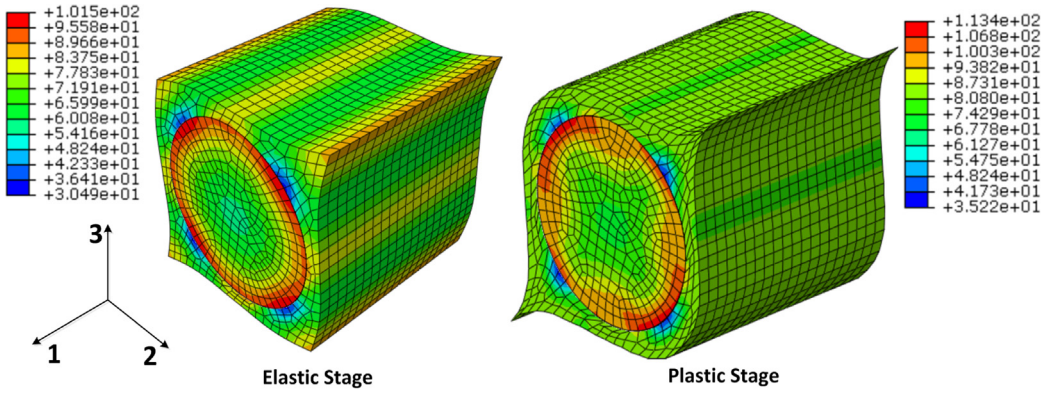

(a) Mises stress

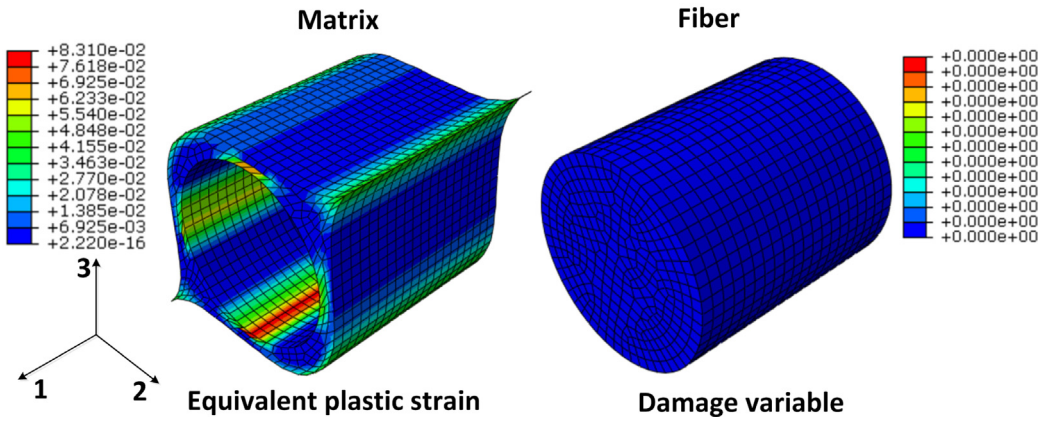

(b) Equivalent plastic strain and damage variable

Fig. 20. Stress, plastic strain and damage distributions of unit cell under transverse shear loading (*23*-direction).

B.4.2. Strain amplification method

An empirical formula for estimating the transverse compressive strength is given by [15, 23, and 24]:

$$F_{2c} = F_{mc}\left[1 - \sqrt{\frac{4V_v}{\pi(1-V_f)}}\right]\left[1 + (V_f - \sqrt{V_f})(1 - \frac{E_m}{E_{f2}})\right] \qquad \text{B.4.2}$$

B.5. Ultimate In-Plane shear strength

B.5.1. Rules of mixtures

It assumed that in-plane shear failure occurs when a transverse crack propagates [15].

$$S = \sqrt{\frac{G_{2c}G_{12}}{\pi(t_t/4)}} \qquad \text{B.5.1}$$

where: G_{2c} is the fracture toughness in mode II.

B.5.2. Fracture mechanic method

Similar to transverse compressive strength, one empirical formula is also adopted [15,23,24].

$$S = S_m\left[1 - \sqrt{\frac{4V_v}{\pi(1-V_f)}}\right]\left[1 + (V_f - \sqrt{V_f})(1 - \frac{G_m}{G_f})\right] \qquad \text{B.5.2}$$

References

[1] A.S. Mosallam, A. Bayraktar, M. Elmikawi, S. Pul, S. Adanur, Polymer composites in construction: an overview, SOJ Mat. Sci. Eng (2015). Open Access.
[2] L.C. Bank, Composites for Construction: Structural Design with FRP Materials, John Wiley & Sons, 2006.
[3] X. Zou, P. Feng, J. Wang, Bolted shear connection of FRP-concrete hybrid beams, J. Compos. Constr. 22 (3) (2018) 04018012.
[4] H. Xin, Y. Liu, A. Du, Thermal analysis on composite girder with hybrid GFRP-concrete deck, Steel Compos. Struct. 19 (2015) 1221–1236.
[5] L. Ascione, J.-F. Caron, P. Godonou, K. van IJselmuijden, J. Knippers, T. Mottram, et al., Prospect for new guidance in the design of FRP: support to the implementation, harmonization and further development of the Eurocodes, Publ. Office Eur. Union (2016).
[6] H. Xin, Y. Liu, A. Mosallam, Y. Zhang, C. Wang, Hygrothermal aging effects on flexural behavior of pultruded glass fiber reinforced polymer laminates in bridge applications, Constr. Build. Mater. 127 (2016) 237–247.
[7] H. Xin, Y. Liu, A. Mosallam, Y. Zhang, Moisture diffusion and hygrothermal aging of pultruded glass fiber reinforced polymer laminates in bridge application, Compos. Part B Eng. 100 (2016) 197–207.
[8] F. Ascione, M. Lamberti, A.G. Razaqpur, S. Spadea, M. Malagic, Pseudo-ductile failure of adhesively joined GFRP beam-column connections: an experimental and numerical investigation, Compos. Struct. 200 (2018) 864–873.
[9] W. Liu, P. Feng, J. Huang, Bilinear softening model and double K fracture criterion for quasi-brittle fracture of pultruded FRP composites, Compos. Struct. 160 (2017) 1119–1125.
[10] T.J. Schniepp, Design manual development for a hybrid, FRP double-web beam and characterization of shear stiffness in FRP composite beams 2002.
[11] H. Xin, A.S. Mosallam, Y. Liu, C. Wang, J. He, Experimental and numerical investigation on assessing local bearing behavior of a pultruded GFRP bridge deck, Compos. Struct. 204 (2018) 712–730.
[12] H. Xin, A. Mosallam, Y. Liu, C. Wang, Y. Zhang, Analytical and experimental evaluation of flexural behavior of FRP pultruded composite profiles for bridge deck structural design, Constr. Build. Mater. 150 (2017) 123–149.

[13] H. Xin, A. Mosallam, Y. Liu, Y. Xiao, J. He, C. Wang, et al., Experimental and numerical investigation on in-plane compression and shear performance of a pultruded GFRP composite bridge deck, Compos. Struct. (2017) 914–932.
[14] H. Xin, Y. Liu, A.S. Mosallam, J. He, A. Du, Evaluation on material behaviors of pultruded glass fiber reinforced polymer (GFRP) laminates, Compos. Struct. 182 (2017) 283–300.
[15] E.J. Barbero, Introduction to Composite Materials Design, CRC Press, 2010.
[16] H.T. Hahn, S.W. Tsai, Introduction to Composite Materials, CRC Press, 1980.
[17] E.J. Barbero, Finite Element Analysis of Composite Materials Using AbaqusTM, CRC Press, 2013.
[18] B.D. Agarwal, L.J. Broutman, K. Chandrashekhara, Analysis and Performance of Fiber Composites, John Wiley & Sons, 2006.
[19] R.M. Jones, Mechanics of Composite Materials. vol. 193, Scripta Book Company, Washington, DC, 1975.
[20] L. Liu, Z.-M. Huang, Stress concentration factor in matrix of a composite reinforced with transversely isotropic fibers, J. Compos. Mater. 48 (2014) 81–98.
[21] V.I. Davydenko, Strength and deformability of reinforced polymers in tension normal to the fibers, Mech. Compos. Mater. 6 (1970) 595–599.
[22] J. Schulz, Maximum stresses and strains in the resin of a filament-wound structure, 1963.
[23] J.W. Weeton, K.L. Thomas, D.M. Peters, Engineers' Guide to Composite Materials, American Society of Metals, 1987.
[24] K.K. Stellbrink, Micromechanics of Composites: Composite Properties of Fibre and Matrix Constituents. vol. 1, Hanser Gardner Pubns, 1996.
[25] C. González, J. LLorca, Mechanical behavior of unidirectional fiber-reinforced polymers under transverse compression: microscopic mechanisms and modeling, Compos. Sci. Technol. 67 (2007) 2795–2806.
[26] J. Fish, Practical Multiscaling, John Wiley & Sons, 2013.
[27] T.J. Vaughan, C.T. McCarthy, Micromechanical modelling of the transverse damage behaviour in fibre reinforced composites, Compos. Sci. Technol. 71 (2011) 388–396.
[28] G. Soni, R. Singh, M. Mitra, B.G. Falzon, Modelling matrix damage and fibre–matrix interfacial decohesion in composite laminates via a multi-fibre multi-layer representative volume element (M 2 RVE), Int. J. Solids Struct. 51 (2014) 449–461.
[29] M. Romanowicz, A numerical approach for predicting the failure locus of fiber reinforced composites under combined transverse compression and axial tension, Comput. Mat. Sci. 51 (2012) 7–12.
[30] H. Xin, M. Nijgh, M. Veljkovic, Computational homogenization simulation on steel reinforced resin used in the injected bolted connections, Compos. Struct. 210 (2019) 942–957.
[31] A.R. Melro, P.P. Camanho, F.M.A. Pires, S.T. Pinho, Micromechanical analysis of polymer composites reinforced by unidirectional fibres: Part II – micromechanical analyses, Int. J. Solids Struct. 50 (2013) 1906–1915.
[32] Z. Ullah, L. Kaczmarczyk, C.J. Pearce, Three-dimensional nonlinear micro/meso-mechanical response of the fibre-reinforced polymer composites, Compos. Struct. 161 (2017) 204–214.
[33] J. Fish, R. Fan, Mathematical homogenization of nonperiodic heterogeneous media subjected to large deformation transient loading, Int. J. Num. Methods Eng. 76 (2008) 1044–1064.
[34] ABAQUS V. 6.14 Documentation. Dassault Syst. Simulia Corp., 2014.
[35] C.A. Coulomb, Essai sur une application des regles des maximis et minimis a quelquels problemesde statique relatifs, a la architecture, Mem. Acad. Roy. Div. Sav. 7 (1776) 343–387.
[36] M.L. Benzeggagh, M. Kenane, Measurement of mixed-mode delamination fracture toughness of unidirectional glass/epoxy composites with mixed-mode bending apparatus, Compos. Sci. Technol. 56 (1996) 439–449.
[37] P.D. Soden, M.J. Hinton, A.S. Kaddour, Lamina properties, lay-up configurations and loading conditions for a range of fibre-reinforced composite laminates, Compos. Sci. Technol. 58 (1998) 1011–1022.
[38] N. Uddin, Developments in Fiber-reinforced polymer (FRP) Composites for Civil Engineering, Elsevier, 2013.
[39] ISO E. 1172. Text-Glass-Reinf. Plast-Prepregs Mould Compd Laminates-Determ Text-Glass Miner-Fill Content-Calcination Methods ISO 1172 1996 1996.
[40] ISO E. 1183-1. Plastics – Methods Determining Density Non-Cell Plastics – Part 1 Immers. Method Liquid Pyknometer Method Titration Method, 2004.
[41] Standardization Administration of the People's Republic of China (SAPRC GB/T3354-1999), Test Method for tensile properties of Oriented Fiber Reinforced Plastics, GB/T3354-1999,, SAPRC, Beijing, China, 2005 (In Chinese) n.d.
[42] K. Schneider, Determination of compressive properties of fibre composites in the in-plane direction according to ISO 14126. Part 1: a round Robin test, Appl. Compos. Mater. 14 (1) (2007) 1–15.
[43] Standardization Administration of the People's Republic of China (SAPRC GB/T28889-2012), Test Method for in-Plane Shear Properties of Composites Materials, GB/T28889-2012, SAPRC, Beijing, China, 2005 (In Chinese).
[44] Association ACM, Pre-standard for Load & Resistance Factor Design (LRFD) of Pultruded Fiber Reinforced Polymer (FRP) Structures, ACMA, USA, Arlington, VA, 2012.
[45] J. Aboudi, Mechanics of Composite Materials: A Unified Micromechanical Approach vol. 29, Elsevier, 2013.